# Assessing the Impact of Positioning Errors in Car-Borne Repeat-Pass SAR Interferometry With a Controlled Rail-Based Experiment

Roberto Coscione , Irena Hajnsek , *Fellow, IEEE*, Charles Werner , *Senior Member, IEEE*, and Othmar Frey , *Senior Member, IEEE*

*Abstract*—Agile synthetic aperture radar (SAR) platforms such as car-borne and UAV-borne SAR systems require combined inertial navigation systems (INS) and global navigation satellite systems (GNSS) to measure the radar sensor trajectories used for focusing and interferometric processing. Measurement inaccuracies from INS/GNSS systems lead to residual phase errors in the SAR products whose minimization is crucial to derive accurate topographic and deformation information. In this work, we analyze the impact of residual positioning errors on car-borne repeat-pass SAR interferometry at L-band for different INS/GNSS measurement configurations and for the typical car-borne acquisition geometry. The positioning errors are evaluated both during single SAR acquisitions with long integration times and between different acquisitions as a function of the distance of the radar platform from the GNSS reference stations. We show the reduction of interferometric phase errors achievable by additionally using a GNSS receiver mounted in the vicinity of the SAR platform as compared to remote reference stations of the national network of permanent GNSS receivers. Test results obtained in a controlled setup with a rail-based SAR system equipped with a navigation-grade INS/GNSS system show maximum repeat-pass trajectory errors on the order of 1–2 cm using a local GNSS reference station and up to 10–15 cm using the remote reference stations, leading to azimuth and range phase trends in the interferometric products.

*Index Terms*—Global navigation satellite system, inertial navigation, measurement errors, radar remote sensing, radar interferometry, synthetic aperture radar, terrain mapping.

## I. INTRODUCTION

ACCURATE knowledge of the trajectory and the orientation of the radar antenna during the SAR data acquisition is a critical requirement for SAR image focusing and interferometric processing [1]–[4]. Especially for agile platforms such as small aircraft, unmanned aerial vehicles (UAV), or road vehicles, which can have highly nonlinear sensor trajectories [5]–[7], accurate positioning data along with topographic information of the mapped area are needed to build the spatially varying matched filter for azimuth focusing and to produce well-focused and motion-compensated SAR and InSAR data based on the 3-D geometry of the mapped scene [5], [8]–[11].

Commonly, position and attitude of the radar platform are measured with positioning measurement systems mounted on board, such as integrated inertial navigation systems and global navigation satellite systems (INS/GNSS) [12]–[14]. The finite accuracy of the positioning measurement system causes a mismatch between the actual sensor trajectory and the measured one, often referred in the literature as residual motion error, that leads to residual phase errors in the focusing and in the interferometric products [9]–[11], [15]–[18]. Since positioning errors are subject to temporal variations, they are especially critical in repeat-pass (differential) interferometric applications.

For agile SAR platforms, factors such as nonlinear sensor trajectories, long integration time, large variation of look angles and range distances [19], [20], and strong topographic variations, further increase the impact of positioning errors on the interferometric phase and derived products [4], [10], [18], [21]. Moreover, in case of strong topographic variations, DEM height errors lead to different range shifts of the target location as a function of the look angle [22].

In a combined INS/GNSS system, the changing GNSS satellite visibility and the atmospheric variations influence the positioning performance. Therefore, the longer the integration time, the higher the probability of experiencing relative positioning errors along the synthetic aperture as a consequence of the time-varying performance of the INS/GNSS system.

To assess the positioning errors in a real acquisition scenario, multiple positioning measurements should be performed while the radar platform repeats exactly the same trajectory over multiple passes [23], [24]. Since a sufficiently accurate repetition of the sensor trajectory is unfeasible with a car-borne, UAV-borne, or airborne system, we performed a controlled repeat-pass experiment with the L-band SAR mounted on a rail

Roberto Coscione is with the Department of Civil, Environmental and Geomatic Engineering, ETH Zürich, 8093 Zürich, Switzerland (e-mail: coscione.roberto@gmail.com).

Irena Hajnsek is with the Department of Civil, Environmental and Geomatic Engineering, ETH Zürich, 8093 Zürich, Switzerland, and also with the Microwaves and Radar Institute, German Aerospace Center, 82234 Wessling, Germany (e-mail: hajnsek@ifu.baug.ethz.ch).

Charles Werner is with the GAMMA Remote Sensing AG, 3073 Gümligen, Switzerland (e-mail: cw@gamma-rs.ch).

Othmar Frey is with the Department of Civil, Environmental and Geomatic Engineering, ETH Zürich, 8093 Zürich, Switzerland, and also with the GAMMA Remote Sensing AG, 3073 Gümligen, Switzerland (e-mail: otfrey@ethz.ch).

Digital Object Identifier 10.1109/JSTARS.2022.3193053

and additionally equipped with a navigation-grade INS/GNSS system [25].

In an INS/GNSS system, the INS measures accelerations with three orthogonal accelerometers and angular velocities with three orthogonal gyroscopes at a high update rate (e.g., 300 Hz). The accelerations and angular velocities have to be mathematically integrated to obtain relative positioning and attitude information, which leads to substantial drifts over time due to accelerometer and gyroscope biases. The role of the GNSS system is to compensate the INS drifts over time (in the order of seconds and longer) via fusion of the INS and the GNSS data, generally performed using a Kalman filter [14], [26]. Therefore, keeping the errors of the GNSS positioning setup as small as possible is key to minimize time-varying positioning errors. In general, error sources of GNSS-based positioning include satellite clock errors, orbit errors, ionospheric and tropospheric path delays, and multipath effects [27]–[30]. Real-time kinematic (RTK) or post-processed kinematic (PPK) GNSS positioning with respect to a reference GNSS station allows to compensate for the first two error sources and using dual-frequency (e.g., L1/L2) GNSS systems a ionosphere-free solution can be obtained.

RTK/PPK also allows to exploit the spatial correlation of the tropospheric path delay in the GNSS signal and to reduce its impact as a function of the distance between the GNSS rover and the reference station (the closer, the better) [31], [32].

Networks of permanent and continuously operating GNSS ground reference stations are available in many countries worldwide, like CORS (continuously operating reference station) in America, EPN (EUREF permanent network) in Europe, and AGNES (automated GNSS network for Switzerland) in Switzerland [33]–[35] but their mean distance from the SAR platform is fixed once the measurement target area is established. Portable GNSS reference stations can be deployed in the vicinity of the SAR platform in an effort to further reduce the tropospheric disturbance, although such option adds additional burden in terms of measurement setup and processing.

In view of operational repeat-pass DInSAR measurements from agile platforms, it is relevant to understand whether using one or more reference stations of the available network of permanent GNSS receivers is sufficient or the local GNSS reference station is required to guarantee high positioning accuracy and, hence, low residual phase errors. Although residual motion compensation [15], [20], [36]–[40] and autofocusing techniques [8], [41]–[48] can, to some extent, reduce the impact of positioning errors, achieving accurate trajectory estimates in the first instance is desirable to minimize aperture- and topography-dependent phase trends.

The aim of this work is to quantify the trajectory errors measured with a high-performance (navigation-grade) INS/GNSS system for different GNSS reference station setups and to analyze their impact on the interferometric phase in a real acquisition scenario relevant to the acquisition geometry of a car-borne SAR system [49]–[53]. In particular, we investigate the effect of the trajectory errors on repeat-pass SAR acquisitions as a function of the distance of the radar platform from different GNSS reference stations. We set up a rail-based SAR and
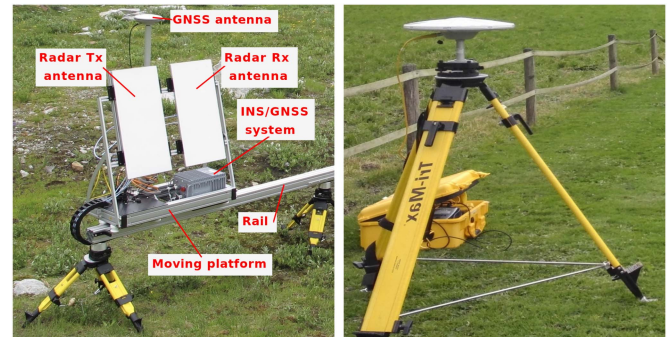


Fig. 1. Left: positioning measurement system and radar antennas mounted on the rail-based platform. Right: local GNSS receiver used as reference station for PPK processing deployed about 10 m away from the radar platform.

INS/GNSS measurement system [25] to guarantee an almost exact repeatability of the platform trajectories over multiple passes and, thus, to quantify the time-varying positioning errors with respect to the actual platform trajectory. We compare the positioning solutions obtained with the closest reference stations of the AGNES network and with a local nonpermanent GNSS receiver deployed few meters away from the SAR platform, and analyze the PPK-only and the integrated INS/PPK positioning solutions.

The residual positioning errors are evaluated during the timeframe of single SAR acquisitions with long integration times and between different passes relevant to InSAR/DInSAR acquisitions. The rail-based setup allows to quantify the effect of positioning errors on the DInSAR data by isolating the residual phase errors from the troposphere-induced interferometric phase (also known as atmospheric phase screen).

Additionally, we report a sensitivity analysis of the interferometric phase to baseline errors to provide a theoretical indication of the interferometric phase errors observable in the typical car-borne acquisition geometry.

The article is organized as follows. Section II presents the experimental measurement setup, the processing scheme adopted for GNSS and INS data integration, the sensitivity analysis to baseline errors, and the strategy employed for the evaluation of the residual interferometric phase errors. Section III reports the results of the analyses of the positioning and the DInSAR measurements. A discussion of the results is provided in Section IV. The conclusions are drawn in Section V.

## II. METHODS

### A. Experimental Measurement Setup

To collect high-quality repeat-pass positioning and attitude data and guarantee an almost perfect repeatability of the platform trajectory in a controlled setup, we performed repeat-pass SAR data acquisitions along a fixed 10-m-long rail additionally equipped with a navigation-grade INS/GNSS system (see Fig. 1). The constrained position of the sensor trajectory along the rail allows to evaluate the accuracy (trueness and precision [23]) of the estimated trajectory with respect to the nominal path of the platform.

TABLE I
TECHNICAL DATA OF THE NAVIGATION-GRADE INERTIAL NAVIGATION SYSTEM (INS) IMAR INAV-RQH-10018 MOUNTED IN THE STRAPDOWN CONFIGURATION ON THE PLATFORM MOVING ALONG THE RAIL

| Accelerometer type | 3 servo accelerometers | Gyroscope type | 3 ring laser gyro |
|---|---|---|---|
| Accelerometer bias | < 25 $\mu$**g** | Gyro bias | < 0.002°/h |
| Accelerometer resolution | < 5 m**g** | Gyro resolution | <0.001°/s |
| Q | < 8 $\mu$**g**/$\sqrt{\text{Hz}}$ | Angular random walk | < 0.0015°/$\sqrt{h}$ |
| Attitude accuracy (unaided) | <0.01° | True heading | < 0.025°/ cos(*lat*) |
| Position accuracy (unaided) | 0.6 nmi/h (~1.1 km/h) | GNSS receiver | Novatel (GPS, GLONASS) |
| Inertial data rate | 300 Hz | GNSS data rate | 1 Hz |

Gyro and accelerometer biases are responsible for the inertial drift and define the performance of the system in absence of external aids (e.g., during a GNSS outage). $g \simeq 9.81$ m/s$^2$.

TABLE II
GNSS STATIONS USED AS REFERENCE FOR CARRIER-PHASE DIFFERENTIAL GNSS PROCESSING (PPK)

| Station name | OALP | HABG | Local |
|---|---|---|---|
| Description | Permanent station of the AGNES network: Oberalppass | Permanent station of the AGNES network: Hasliberg | Stationary non-permanent (portable) receiver. |
| Antenna type | TRM59800.00 | TRM59800.00 | TRM77971.00 |
| Baseline | ~20 km | ~20 km | < 10 m |
| Height | 2139.53 m | 1147.97 m | 2000.37 m |



Fig. 2. Photograph of the Stein Glacier acquired during the measurement campaign, July 2018.

The measurement setup includes the following elements (see Fig. 1).

1) A platform moving along a 10-m-long rail at a speed of about 40 cm/s controlled by a motor synchronized with the radar transmissions. Start and end positions of the platform are the same for every pass.

2) A linearly frequency modulated continuous wave (FMCW) radar system operating at L-band with a bandwidth of 100 MHz and a chirp length of 2 ms (PRF 500 MHz) [52].

3) Two radar antennas (one transmitting and one receiving) rigidly mounted to the moving platform, with 3 dB beamwidth of 40° in azimuth and 20° in elevation.

4) A INS/GNSS system and a GNSS antenna fixed to the platform moving along the rail (strapdown configuration [14]). Table I summarizes the specifications of the INS/GNSS system.

5) A nonpermanent stationary GNSS receiver (see Fig. 1) steadily mounted few meters away from the rail (in the following indicated as "local reference station") used as reference station for differential GNSS processing.

6) Two permanent, continuously operating, stationary GNSS reference stations of the AGNES network [35], located at different heights at a distance of about 20 km from the rail (see Table II), used for GNSS differential processing.

The moving GNSS receiver—called "rover" in the GNSS jargon—and the reference stations are dual-frequency and multiconstellation (GPS and GLONASS).

The radar acquisitions were performed at every pass during the forward movement of the platform. Position, velocity, and attitude measurements were performed for the entire duration of the campaign at a data acquisition rate of 1 Hz for the GNSS and 300 Hz for the INS.
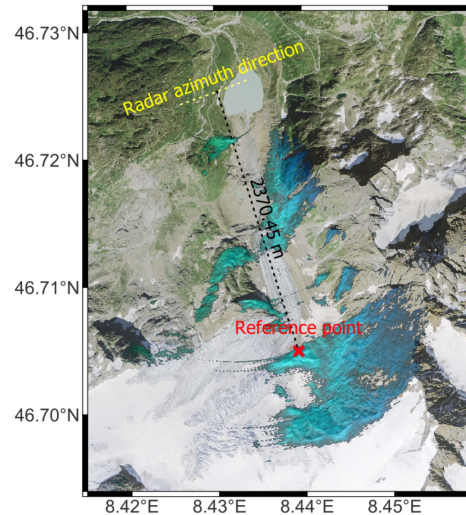


Fig. 3. Map of the imaged area (Stein glacier) located at a distance from the radar ranging roughly from 400 to 3200 m for a total area of 2.6 km$^2$. The straight dotted yellow line indicates the direction of the rail (the length is exaggerated to highlight the azimuth direction of the radar). North is upwards. The interferometric reference point (red cross) is set on an exposed rock at a distance of about 2370 m from the rail midpoint. swisstopo geodata.

The measurement campaign took place in July 2018 in the Bernese Alps, where radar acquisitions of the Steingletscher (Stein glacier) were performed from a distance of about 3200 m from the target area (see Figs. 2 and 3). The height difference between the radar position and the top part of the mapped area

is about $1200\,\mathrm{m}$, corresponding to a variation of look angles between near range and far range of $20°$.

### B. Trajectory Estimation via GNSS and INS Data Processing

To retrieve the trajectory information required to focus the SAR data, inertial and GNSS data were integrated in postprocessing to reduce the accumulation error affecting accelerometers and gyroscopes of the INS. First, for each reference station, the GNSS measurements were processed using the carrier-phase differential GNSS technique known as postprocessed kinematic (PPK) [30], [54], which provides the time-series of platform positions for the entire duration of the measurement campaign. The PPK solutions were then integrated with the inertial data via a loosely coupled extended Kalman filter followed by a Rauch–Tung–Striebel (RTS) smoother [26], [55], [56]. In the following, we refer to the integrated and smoothed INS/PPK positioning solutions, which were then used for SAR focusing, as RTS solutions.[1]

The PPK positioning solutions and, hence, the related RTS ones were independently calculated for each reference station indicated in Table II:

1) Two solutions are based on the local reference station located less than $10\,\mathrm{m}$ away from the rover using single-frequency and dual-frequency processing, respectively. The coordinates of the local reference station were calculated via static carrier-phase differential processing using one of the AGNES stations as reference, specifically the one with the lower altitude difference with respect to the rover (the OALP station of Table II).
2) One solution is based on the "OALP" AGNES reference station (dual-frequency).
3) One solution is based on the "HABG" AGNES reference station (dual-frequency).
4) One solution is based on both the OALP and the HABG AGNES stations used at the same time (dual-frequency).

In the case of the AGNES reference stations, dual-frequency processing proved necessary to reduce the ionospheric effect on the received data and obtain integer carrier-phase ambiguity solutions [30], [57]. A processing elevation mask of $15°$ was used to exclude highly attenuated signals transmitted from satellites visible at low-elevation angles and to reduce multipath.

To calculate the nominal radar trajectory, we retrieved each trajectory relevant to the radar acquisitions from the single-frequency local RTS solution (local_L1), for a total of 58 trajectories that were then averaged together. The average trajectory is a good approximation of the actual shape of the rail that, given its length and the mounting system based on tripods, slightly deviates in altitude from a perfectly linear trajectory. By averaging the available trajectories, we exploited the redundancy of the repeat-pass positioning data offered by the constrained position of the moving platform. The repeated trajectories are separated by a temporal baseline of at least 2 min for an overall time window of more than 2 h and are, therefore, mostly

---

[1]PPK processing performed with the commercial software Novatel GrafNAV 8.70. Kalman filter and RTS smoother used for INS/PPK integration provided by iMAR Navigation GmbH.

TABLE III
GNSS REFERENCE STATIONS AND CARRIER SIGNALS
USED FOR PPK PROCESSING

| Reference station | Carrier | Legend entry |
|---|---|---|
| local station | L1 | local_L1 |
| local station | L1+L2 | local_L1L2 |
| AGNES: OALP | L1+L2 | OALP |
| AGNES: OALP + HABG | L1+L2 | 2agnes |
| AGNES: HABG | L1+L2 | HABG |

The column "legend entry" indicates the name used in the plots for the PPK and the related RTS positioning solutions.

uncorrelated [58], [59]. Hence, the standard deviation of the average trajectory is at least one order of magnitude lower than the individual trajectories.

### C. Radar Processing and "Self-Interferograms"

Together with a digital elevation model (DEM) of the mapped area, the integrated RTS trajectories were used for SAR focusing via time-domain back-projection (TDBP). The TDBP focusing algorithm [6], [60]–[64] can be used for any nonlinear trajectory and produces motion-compensated, coregistered, and geocoded SLCs. Since in TDBP, the topographic phase is removed by means of the DEM and the trajectory information, the interferometric combination of two focused images automatically produces a differential interferogram [18], [65].

Nevertheless, as for other focusing algorithms, the correctness of the focusing is limited by the accuracy of the positioning system (INS/GNSS) [22]. Due to trajectory estimation errors, different from pass to pass, the interferometric phase contains residual phase components originating from the presence of a baseline error that varies with range and azimuth. The trajectory errors, and hence the residual phase, depend on the distance to the reference station used for the differential GNSS processing.

To show the effect of trajectory errors on the differential interferometric phase for different GNSS setups, we exploited the inherent zero spatial baseline of the rail-based system. Specifically, first we performed TDBP focusing of the raw radar data, acquired from the rail-based system, using the nominal sensor trajectory and the different RTS trajectories, namely the trajectories based on the local reference station and the ones based on the vertically closer AGNES reference station (indicated as local_L1 and OALP in Table III, respectively). Then, we created a set of differential interferograms using the data focused with the nominal trajectory as primary and the data focused with each RTS trajectory as secondary. We refer to this nonstandard interferometric product as "self-interferograms."

A simple model for the self-interferograms can be derived from the repeat-pass DInSAR phase:

$$\varphi_{DInSAR} = \varphi_{\mathrm{def}} + \varphi_{\mathrm{pos}} + \varphi_{\mathrm{tropo}} + \varphi_{\mathrm{DEM}} + \varphi_{\mathrm{noise}}, \quad (1)$$

where $\varphi_{\mathrm{def}}$ is the deformation signal of interest, $\varphi_{\mathrm{pos}}$ is the residual phase due to positioning errors, $\varphi_{\mathrm{tropo}}$ is the tropospheric path delay (also known as atmospheric phase screen), $\varphi_{\mathrm{DEM}}$ is the residual phase due to DEM errors, and $\varphi_{\mathrm{noise}}$ includes thermal noise and other unmodeled noise sources.

Since the self-interferograms are generated from image pairs relevant to the same raw data, the temporal baseline is zero and both the deformation and the tropospheric phase components cancel out in the interferogram ($\varphi_{\text{def}} = \varphi_{\text{tropo}} = 0$). Therefore, only the effect of baseline and DEM errors affect the phase of the self-interferogram $\varphi_{\text{self}}$:

$$\varphi_{\text{self}} = \varphi_{\text{pos}} + \varphi_{\text{DEM}} + \varphi_{\text{noise}}. \tag{2}$$

Note that such experiment involving the creation of self-interferograms is only possible with systems physically constrained in two dimensions, such as the rail-based one, equipped with a positioning system, which is usually not necessary for rail-based systems [66]–[68]. The same radar and INS/GNSS systems are employed on the car-borne SAR.

In addition to the self-interferograms, canonical repeat-pass differential interferograms were also created using the nominal trajectory, the RTS local_L1 trajectories, and the RTS OALP trajectories, respectively.

Regarding the resolution of the rail-based interferograms, the slant-range resolution is defined by the radar bandwidth while the azimuth resolution depends on the range and the rail length, that is:

$$\Delta_{rg} = \frac{c}{2B_W} \tag{3}$$

$$\Delta_{az} = \frac{\lambda}{2L}r, \tag{4}$$

where $L$ is the length of the synthetic aperture that can be obtained on the rail, $\lambda$ is the radar wavelength, $r$ is the slant range, and $B_W$ is the chirp bandwidth. As it is typical for a rail-based SAR system [66]–[68], whose length is usually smaller than the azimuth extension of the radar footprint on the scene, the resolution is not constant with the range. With $L = 10\,\text{m}$, $\lambda = 22.6\,\text{cm}$, and $r$ between 400 m and 3.2 km, the azimuth resolution varies between 4.5 and 35 m from near-range to far-range, while the range resolution is 1.5 m for a bandwidth of $B_W = 100\,\text{MHz}$. The DEM posting is 1 m and a multilooking windows of $35 \times 35$ pixels were applied.

### D. Sensitivity Analysis

In this section, a sensitivity analysis of the interferometric phase to baseline errors is reported. For a generic target, the interferometric phase $\varphi$ is related to the range difference $\delta r$ measured between two SAR acquisitions [69], [70]

$$\varphi = \frac{4\pi}{\lambda}\delta r. \tag{5}$$

In this case, only the geometric component of the interferometric phase is taken into account. From the geometry depicted in Fig. 4, the following equation is obtained using the law of cosines:

$$(r + \delta r)^2 = r^2 + B^2 - 2\,r\,B\,\sin\left(\theta - \alpha_B\right), \tag{6}$$

where $r$ is the slant range, $\theta$ is the target look angle, $B$ is the baseline length, and $\alpha_B$ is the baseline tilt angle.
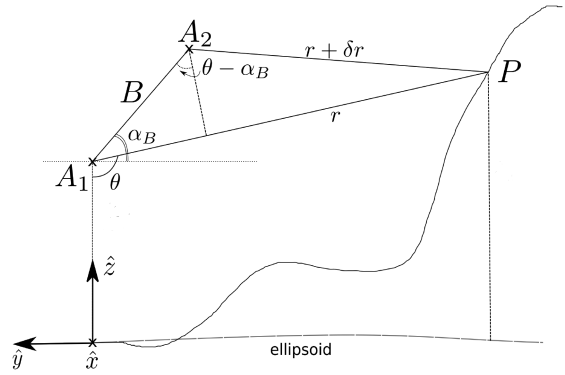


Fig. 4. Acquisition geometry of the car-borne SAR systems. A1 and A2 indicate the antenna positions for two different passes. $B$ is the baseline length, $\alpha_B$ is the baseline tilt angle, $\theta$ is the look angle, $r$ is the range distance, $\delta r$ is the range difference between the two passes. The geometry is also valid for the rail-based experimental setup (with $B = 0$).

Substituting (6) in (5), it follows:

$$\varphi = \frac{4\pi}{\lambda}\left(\sqrt{r^2 + B^2 - 2rB\sin\left(\theta - \alpha_B\right)} - r\right). \tag{7}$$

Using the error propagation formula truncated to the first order [71], the phase error due to baseline and roll errors is given by:

$$\sigma_\varphi^2 \simeq \left(\frac{\partial\varphi}{\partial B}\right)^2 \cdot \sigma_B^2 + \left(\frac{\partial\varphi}{\partial\alpha_B}\right)^2 \cdot \sigma_{\alpha_B}^2, \tag{8}$$

where $\sigma_\varphi^2, \sigma_B^2$, and $\sigma_{\alpha_B}^2$ are the variance of the phase, the baseline length, and the baseline tilt angle, respectively.

From (7), the first derivatives of the phase with respect to baseline length and the tilt angle are

$$\frac{\partial\varphi}{\partial B} = \frac{4\pi}{\lambda}\frac{B - r\sin\left(\theta - \alpha_B\right)}{\sqrt{r^2 + B^2 - 2rB\sin\left(\theta - \alpha_B\right)}}$$

$$\frac{\partial\varphi}{\partial\alpha_B} = \frac{4\pi}{\lambda}\frac{Br\cos\left(\theta - \alpha_B\right)}{\sqrt{r^2 + B^2 - 2rB\sin\left(\theta - \alpha_B\right)}}. \tag{9}$$

Substituting (9) in (8), and considering alternatively the baseline length error and the baseline tilt angle error, it follows:

$$\sigma_{\varphi|\sigma_{\alpha_B}=0} \simeq \frac{4\pi}{\lambda}\left|\frac{B - r\sin\left(\theta - \alpha_B\right)}{\sqrt{r^2 + B^2 - 2rB\sin\left(\theta - \alpha_B\right)}}\right|\sigma_B$$

$$\sigma_{\varphi|\sigma_B=0} \simeq \frac{4\pi}{\lambda}\left|\frac{Br\cos\left(\theta - \alpha_B\right)}{\sqrt{r^2 + B^2 - 2rB\sin\left(\theta - \alpha_B\right)}}\right|\sigma_{\alpha_B}. \tag{10}$$

Equations (10) are plotted in Fig. 5 as a function of the look angle for different baseline errors and tilt angle errors. The nominal baseline is $B = 0.5\,\text{m}$, while the nominal tilt angle $\alpha_B$ is either $0°$ or $90°$ to simulate horizontal baseline and vertical baselines, respectively. Note that the tilt angle error $\sigma_{\alpha_B}$ is zero if the nominal baseline is zero but can lead to very large phase errors even for small baselines, depending on the look angle.

In practice, especially in DInSAR applications, the interferometric phase is always calculated with respect to a (stable) reference point located in the imaged area and therefore
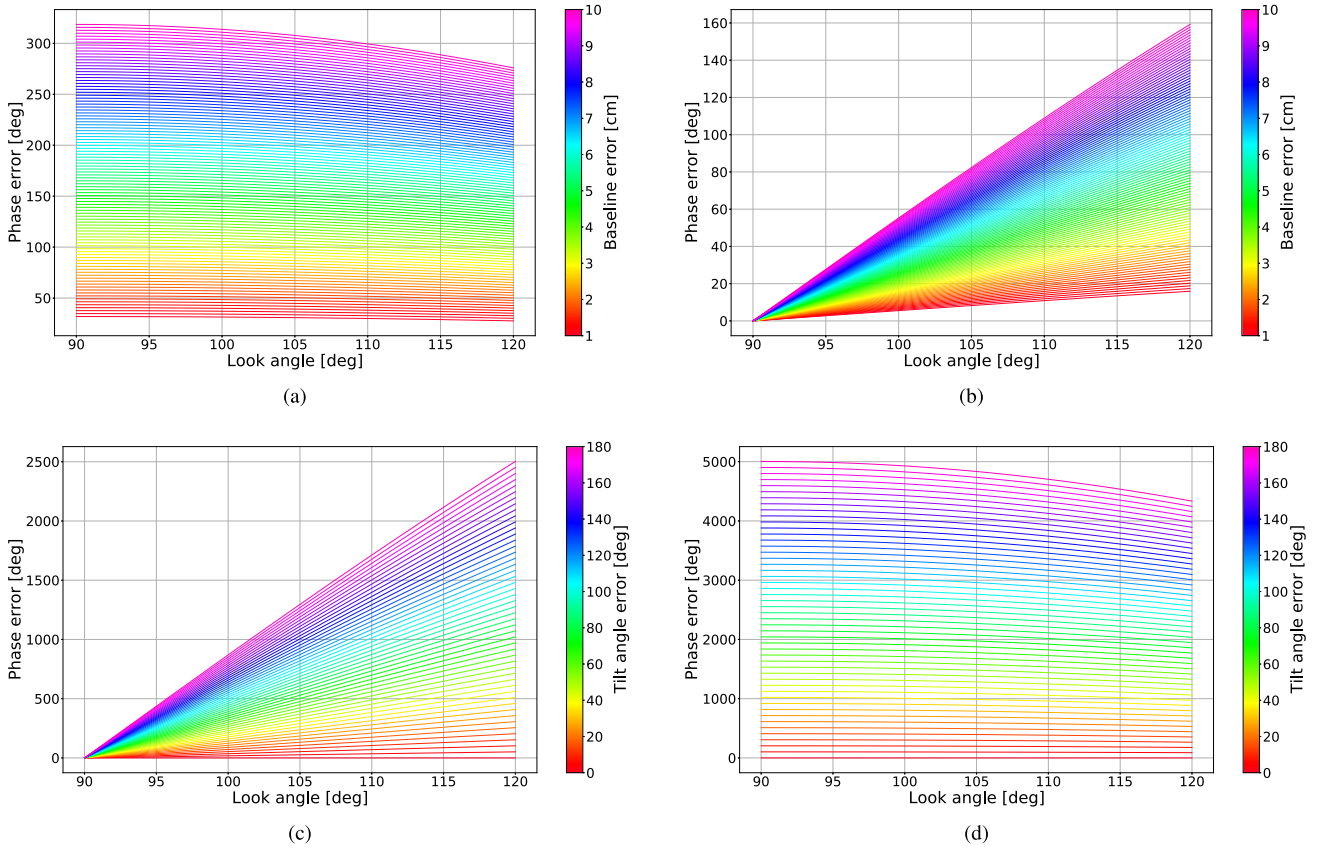
Fig. 5. Absolute interferometric phase error versus the look angle for different baseline length errors and baseline tilt angle errors. Range distance $r = 2000\,\mathrm{m}$. Nominal baseline $B = 0.5\,\mathrm{m}$. $\alpha_B$ is the nominal baseline tilt angle. $\sigma_{\alpha_B}$ is the baseline tilt angle error. $\sigma_B$ is the baseline error. (a) $\alpha_B = 0°, \sigma_{\alpha_B} = 0$. (b) $\alpha_B = 90°, \sigma_{\alpha_B} = 0$. (c) $\alpha_B = 0°, \sigma_B = 0$. (d) $\alpha_B = 90°, \sigma_B = 0$.

only the relative phase error is of interest. The latter is zero on the reference point and increases for points located away from the reference as the look angle and the baseline error vary, leading to potential errors up to $50°–100°$. Note that, in practice, the baseline error may vary along azimuth as a consequence of the time-varying nature of the positioning errors, which is particularly relevant in the case of long integration times, causing differing phase trends [72].

Although the plots in Fig. 5 are reported for a fixed range distance ($r = 2000\,\mathrm{m}$), due to the small nominal baseline, which is typical for car-borne SAR acquisitions, the variation of the phase error with the slant range is minimal and mostly occurs in close range. This can be shown by using the plane wave (or parallel waves) approximation [69], valid for $\delta r \ll r$ and $B \ll r$, for which (7) becomes

$$\varphi_{\mathrm{pwa}} \simeq -\frac{4\pi}{\lambda} B \sin\left(\theta - \alpha_B\right). \tag{11}$$

Using (11), the phase derivatives in (9) become:

$$\frac{\partial \varphi_{\mathrm{pwa}}}{\partial B} = -\frac{4\pi}{\lambda} \sin\left(\theta - \alpha_B\right)$$

$$\frac{\partial \varphi_{\mathrm{pwa}}}{\partial \alpha_B} = \frac{4\pi}{\lambda} B \cos\left(\theta - \alpha_B\right), \tag{12}$$

showing that there is no direct dependence from the range distance of the phase sensitivity to baseline errors. Note, however, that the look angle $\theta$ varies with range due to the topographic height changes and to the side-looking geometry of the SAR [73]. In the presence of strong topographic changes, large variations of look angles can occur, especially in close range, resulting in significant relative phase errors in function of the baseline errors.

To verify in which range of values (relevant for a car-borne acquisition scenario) the plane wave approximation holds, let us consider the approximation error $\epsilon_\varphi$ [69]:

$$\epsilon_\varphi = \varphi - \varphi_{\mathrm{pwa}}$$

$$= \frac{4\pi}{\lambda} \sqrt{r^2 + B^2 - 2rB \sin\left(\theta - \alpha_B\right)}$$

$$- r + B \sin\left(\theta - \alpha_B\right). \tag{13}$$

Equation (13) is plotted in Fig. 6 for a nominal baseline $B$ of $0.5\,\mathrm{m}$ and shows that the approximation error $\epsilon_\varphi$ is below few degrees for range distances of 100 m and rapidly decreases for larger distances, thus indicating the validity of the plane wave approximation in most range values of interest due to the small nominal baseline length.
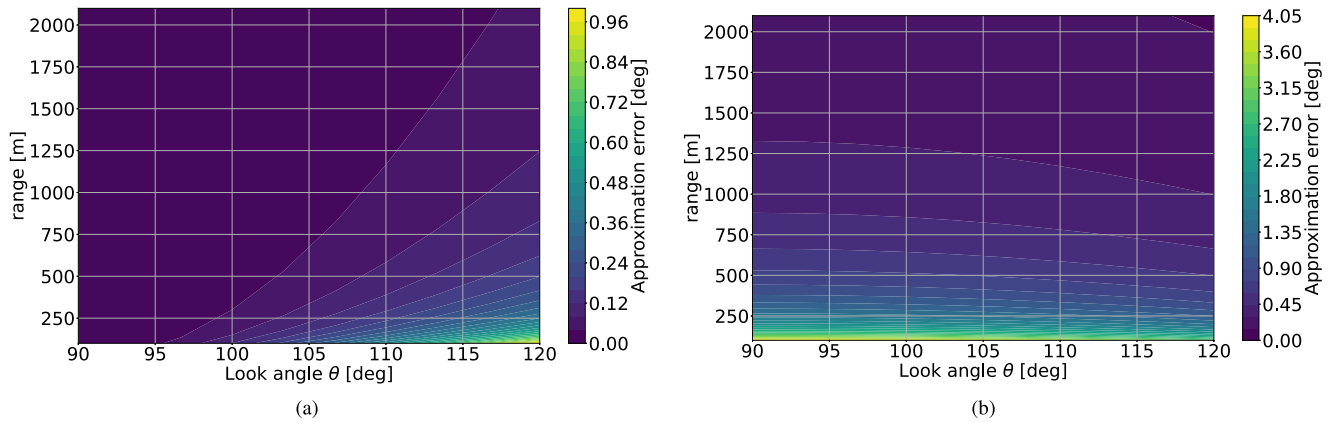
Fig. 6. Phase approximation error owed to the plane wave approximation [see (13)] with varying look angles and range distances for two different values of the nominal baseline tilt angle $\alpha_B$. Nominal baseline $B = 0.5$ m. (a) $\alpha_B = 0°$. (b) $\alpha_B = 90°$.

## III. RESULTS

In this section, we present the results of the rail-based INS/GNSS and InSAR test measurements, highlighting the positioning errors within the time-span of the synthetic aperture and between repeated SAR acquisitions assessed for different configurations: AGNES and local reference stations, PPK-only, and integrated INS/PPK data. Table III reports the nomenclature used in the plots for the different cases.

Fig. 7(a) shows the number of GPS and GLONASS satellites simultaneously visible from the rover moving along the rail and each reference station. For all solutions, the number of satellites is well above the minimum number required to perform differential GNSS processing (5 satellites for dual-constellation GNSS). Fig. 7(b) reports the positional dilution of precision (PDOP), which is an indication of the relative geometrical configuration between ground receivers and satellites. The PDOP value is below 2.4 for each reference station indicating good satellites visibility [30], [54].

The estimated position standard deviation is shown in Fig. 8 for the dual-frequency PPK solutions obtained with the local reference station (local_L1L2) and the closest AGNES reference station (OALP), respectively, and is roughly two times larger for the latter as compared to the former. The standard deviation of the vertical component is worse compared to the horizontal components, as it is usually the case for GNSS data [31].

Fig. 9 shows the time-series of the rover altitude of the PPK-only and the RTS positioning solutions obtained with the different GNSS reference stations, during a time interval of almost 3 h. Standstill epochs are visible at the beginning and at the end of the measurements. The repeated passes of the platform along the rail are indicated by the 30 cm altitude variations with respect to the standstill position (located at an altitude of about 2000.53 m). The solutions obtained with the local reference station (both single-frequency and dual-frequency ones) show a better repeatability of the altitude over the multiple passes and during the standstill periods. On the other hand, decimeter-level time-varying undulations are visible in the positioning solutions obtained with the remote AGNES reference stations.
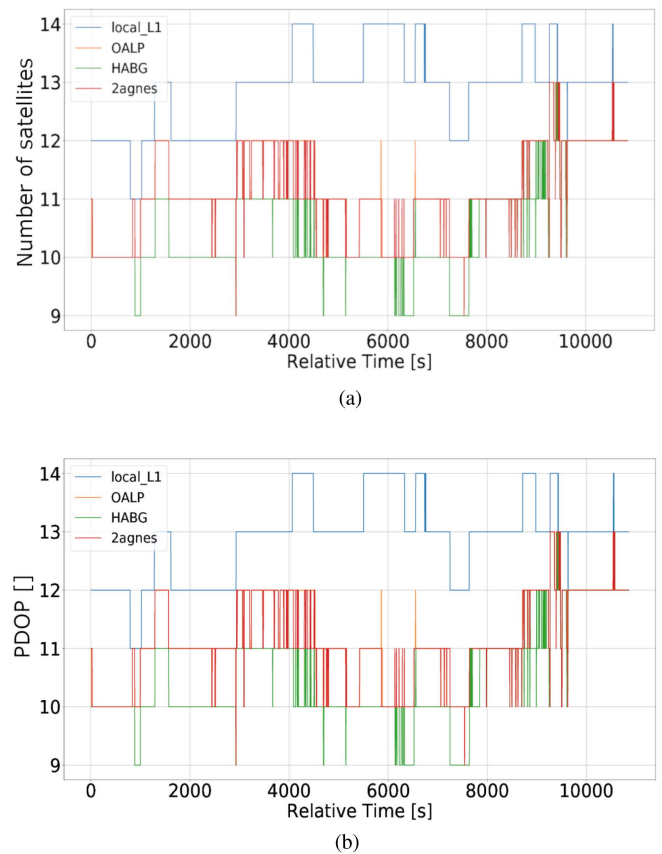


(a)



(b)

Fig. 7. (a) Number of GPS and GLONASS satellites visible at the same time from the rover and the indicated reference station (the local_L1L2 case is the same as local_L1, hence not shown). The number of satellites is above the recommended values in all cases, with the local reference station showing a slightly higher number. (b) positional dilution of precision (PDOP, dimensionless), which is an indication of the relative geometrical configuration between receivers and satellites. Lower values indicate better performance. All solutions present a good value for the PDOP with the local one showing better results.

Fig. 10 shows the boxplots of each PPK-only and the related RTS positioning solutions computed during the static epochs at the beginning and at the end of the campaign for a total time of 30 min (from relative time 0 s to 800 s and from about 9000 s
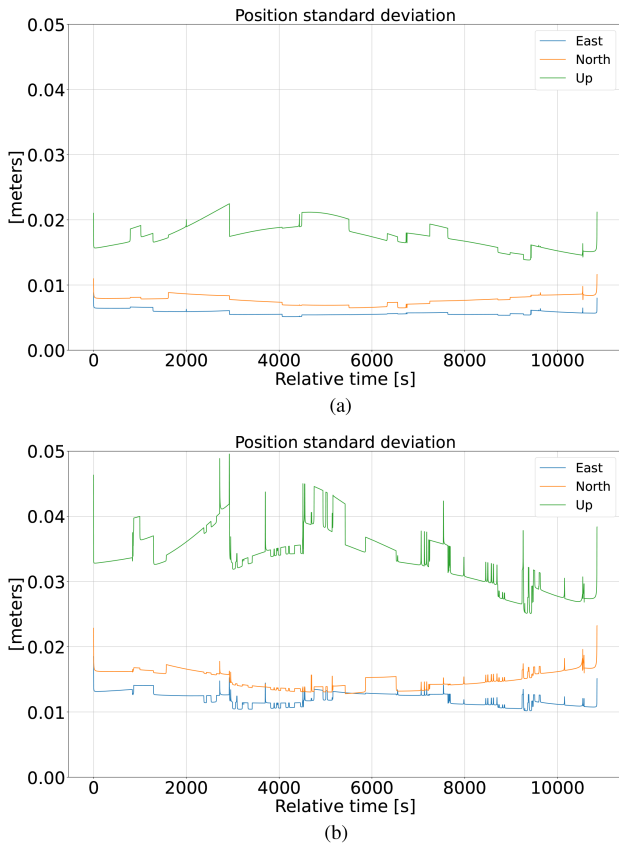
Fig. 8.  Estimated GNSS position standard deviation in East North Up coordinates of the dual-frequency PPK positioning solutions obtained using the local reference station [(a): local_L1L2] and a remote reference station of the permanent AGNES network [(b): OALP]. (a) Local_L1L2. (b) OALP.

to 10000 s in Fig. 9) when the platform stands still in the same position and, hence, any position variation can be directly recognized as error. The better accuracy of the positioning solutions obtained with the local reference station (both single frequency and dual frequency) compared to the ones obtained with the remote reference stations is clearly visible. The OALP solutions (both PPK and RTS) show a median value comparable to the local_L1L2 ones, but a level of precision six times worse (with reference to the interquartile range indicated by the box). The solutions obtained with the HABG reference station present an offset of about 5 cm for the median altitude compared to the OALP ones, which reduces to about 2.5 cm for the solutions using both the OALP and the HAGB reference stations (labelled as 2agnes in the plots).

The positioning accuracy during the kinematic periods, relevant to the repeated passes of the radar along the rail, is visible in Figs. 11 and 12 reporting the deviations from the nominal trajectory. Both the single-frequency and the dual-frequency positioning solutions obtained with the local reference station show a positioning error about 4–5 times smaller than the (dual-frequency) ones obtained with the two AGNES reference stations, which also present an average offset of about 7 cm in the North component [visible in Fig. 12(c) and 12(d)]. The HABG solution additionally shows an average altitude offset of about 8 cm.

The plots in Fig. 11 show the temporal variability of the altitude errors for the RTS local_L1 and the RTS OALP trajectories relevant to the repeat-pass radar acquisitions (i.e., during the forward movement of the platform). The lines are chronologically ordered and color-coded based on their acquisition time to highlight time-related error trends. In the case of the local reference station, the pass-to-pass altitude error is mostly contained within a 1 cm interval with a maximum of 2.2 cm [see Fig. 11(a)] while, in the case of the OALP AGNES reference station, the error spreads over a range of 12 cm [see Fig. 11(b)]. During the 27 s of synthetic aperture time, the variation of the altitude error between the beginning and the end of the acquisitions is mostly subcentimeter in the case of the local_L1 trajectory and around 1–1.5 cm in the case of the OALP trajectory, corresponding to a virtual inclination of the rail of less than 0.1°.

The residual interferometric phase errors due to positioning errors are highlighted in Fig. 13 showing repeat-pass differential interferograms generated from acquisition pairs focused with the nominal quasi-linear trajectory and with the integrated INS/PPK trajectories obtained with the local reference station and with the OALP reference station (RTS local_L1 and RTS OALP, respectively). Three different temporal baselines are reported. The interferometric reference point is set on an exposed rock at a distance of about 2370 m from the rail midpoint (see Fig. 3). The color map is limited to ±0.5 radians to enhance the visibility of the phase errors (out-of-range values are wrapped). In the case of the RTS local_L1 trajectories, the interferometric phase patterns are almost identical to the case of the nominal trajectory while different time-varying phase trends are visible in the case of the RTS OALP trajectories [see Figs. 13(g), 13(h), and 13(i)].

The geocoded self-interferograms are reported in Fig. 14 and show the (differential) phase error caused by positioning errors, without the additional phase components related to the glacier flow and to the tropospheric phase gradient thanks to the zero temporal baseline (as explained in Section II-C). The positioning errors of the RTS local_L1 trajectories mostly cause small scale phase noise [see Figs. 14(a), (c), (e)] or a mild azimuth phase trend of less than 5°–10°. Conversely, the RTS OALP trajectories cause large phase trends affecting the entire mapped area, with phase errors up to 60°–90° with respect to the reference point, predominantly in azimuth [see Figs. (b), (d), and (f)].

## IV. DISCUSSION

The strong correlation between the long-term behavior of the integrated INS/PPK positioning solutions and the long-term behavior of the PPK-only solutions (see Figs. 9 and 12) highlights the importance of accurate differential GNSS processing also when a high-performance INS is employed (as in the present test): the navigation-grade INS provides measurements of relative position and attitude through integration of accelerations and angular velocities, which are available with high accuracy on a short term interval and at a high update rate (300 Hz), but the INS-based positioning and attitude solution drifts with time. Through fusion with the GNSS PPK-based positioning solution, the drift of the INS-navigation is compensated. Therefore, the (smoothed) GNSS PPK-based positioning solution dominates
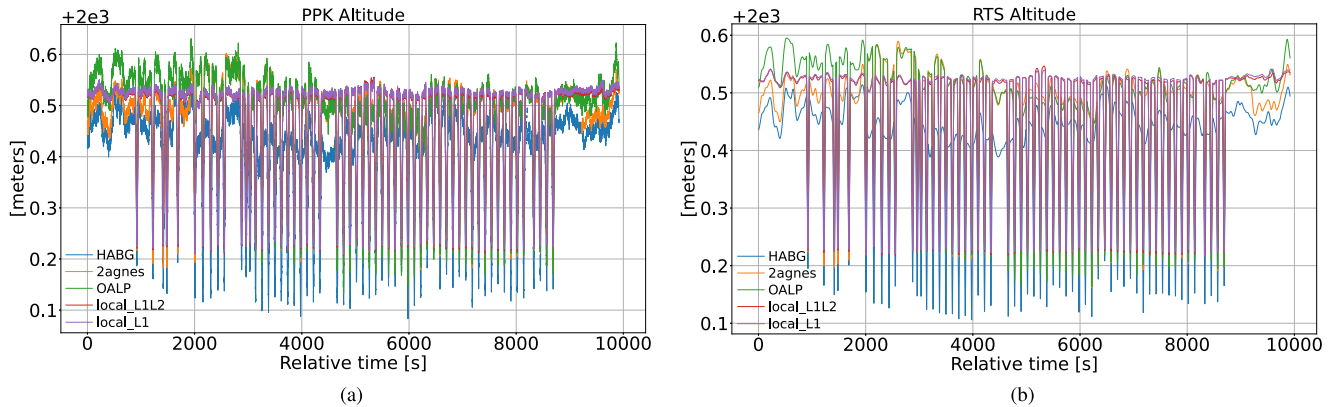
Fig. 9. Altitude time-series (WGS84) of the repeated passes of the platform along the rail for a time span of about 3 h, including standstill periods at the beginning and at the end. Positioning solutions obtained with the local and the AGNES reference stations (see Table III) as well as PPK-only (a) and the integrated RTS (b) solutions are shown. The repeated passes of the platform along the rail are indicated by the altitude variation of about 30 cm with respect to the standstill position.
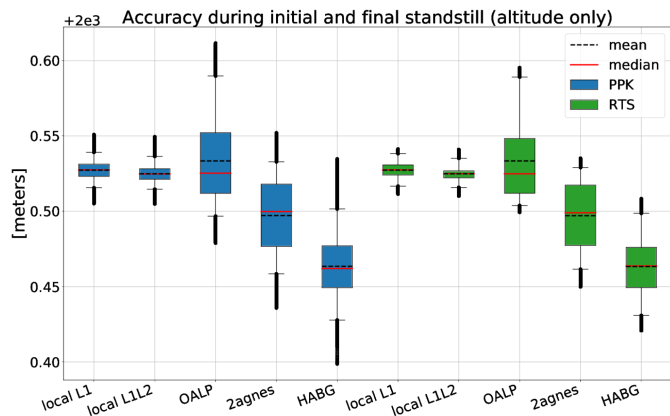


Fig. 10. Accuracy of the geodetic altitude (WGS84) of all the PPK and RTS solutions (see Table III) during initial and final standstill for a total of 30 min of static acquisitions. The standstill position is at an altitude of 2000.53 m. The boxes indicate 50% of the values, the whiskers indicate 5% and 95% percentiles. The solutions obtained with the local reference station outperform the ones obtained with the AGNES reference stations.

the long-term positioning accuracy relative to the GNSS reference station and any uncompensated tropospheric path delay affecting the post-processed GNSS positions plays a major role on the long-term positioning accuracy of the integrated solution, ultimately affecting the repeat-pass spatial baseline error.

The trajectories obtained with the remote (AGNES) reference stations show large altitude undulations due to the uncompensated tropospheric path delays (see Fig. 9), resulting in altitude offsets over repeated passes, as visible in Fig. 11(b), which, in presence of a perpendicular baseline between the SAR acquisitions as in a car-borne or UAV-borne acquisition scenario, would lead to residual topographic errors. The correlation of the tropospheric effect on GNSS signals over short time intervals may lead to comparable errors affecting consecutive passes, as the partial concentration of lines with similar colors in Fig. 11(b) suggests. The worse performance of the solutions involving the HABG reference station as compared to the OALP one

is consistent with larger uncompensated tropospheric errors due to the considerable height difference of the HABG station from the rover (see Table II). On the other hand, positioning offsets and error trends are substantially reduced by using the local reference station, since the tropospheric path delays cancel out thanks to the proximity of the rover and the reference station. Consequently, a more consistent repeatability of the estimated platform trajectories over multiple passes can be achieved by using a local reference station, which is of considerable importance in the context of repeat-pass DInSAR applications.

Residual interferometric phase errors are visible in the differential interferograms as a consequence of the baseline errors caused by the uncertainty of the integrated INS/PPK trajectories. In the case of trajectories calculated with respect to the local reference station, the positioning errors account only for a fraction of the radar wavelength (about $\lambda/10$), consistent with the small-scale phase noise visible in the related self-interferograms [see Fig. 14(a), (c), and (e)].

Conversely, errors up to half wavelength are obtained with the remote reference station, causing the phase error trends visible in both the differential interferograms and in the self-interferograms. The phase trends are comparable to the ones resulting from a misalignment of the rail between different acquisitions, for example, due to repositioning errors of the rail during different campaigns in discontinuous measurements mode [72], [74]–[76]. Larger phase errors are visible on the left flank of the valley where stronger look angle variations occur and where the distance from the interferometric reference point is larger.

In the rail-based configuration, the actual spatial baseline between the acquisitions is practically zero (besides small potential vibrations of the radar antennas) due to the constrained movement of the platform. Therefore, only negligible residual topographic phase variations are left in the differential interferograms as a consequence of baseline and DEM errors. This is consistent with the predominance of azimuth phase trends in the self-interferograms as compared to phase errors in range. On the other hand, in a car-borne repeat-pass acquisition scenario, DEM
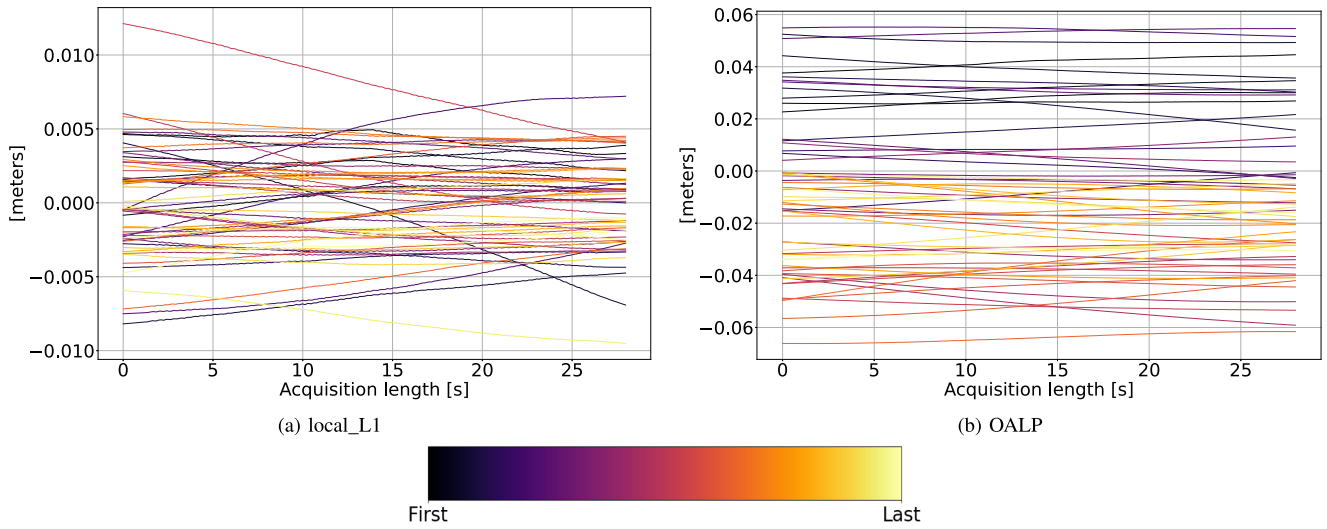
Fig. 11. Deviation from the nominal trajectory (altitude only) of each individual repeat-pass trajectory (RTS solutions) obtained with the local reference station (local_L1) and the AGNES reference station (OALP). The trajectories are chronologically ordered according to their acquisition time and the error lines are sequentially color-coded (see colorbar). Note the different scale of the y-axis in the plots. (a) local_L1. (b) OALP.
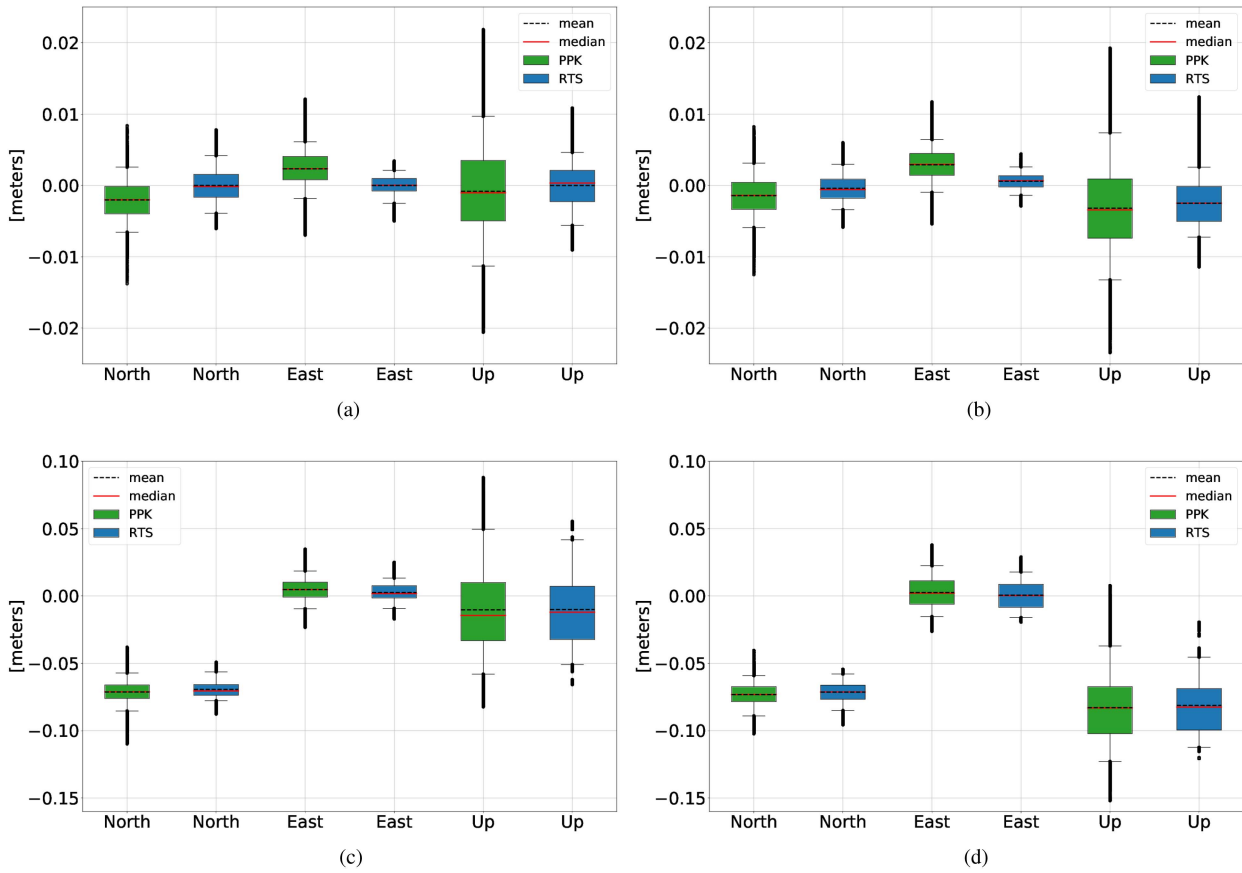


Fig. 12. Accuracy of the PPK-only and the RTS (integrated INS/PPK) radar trajectories during the movement of the platform obtained with the local and the AGNES reference stations. The accuracy is indicated as the variation around the nominal trajectory. The boxes indicate 50% of the values, the whiskers indicate 5% and 95% percentiles. The coordinate system is the Cartesian East, North, Up with origin on the local reference GNSS receiver. Note that the range of values of the ordinate axis is 5 cm in Fig. 12(a) and 12(b) and 25 cm in Fig. 12(c) and 12(d). (a) local_L1. (b) local_L1L2. (c) OALP. (d) HABG.
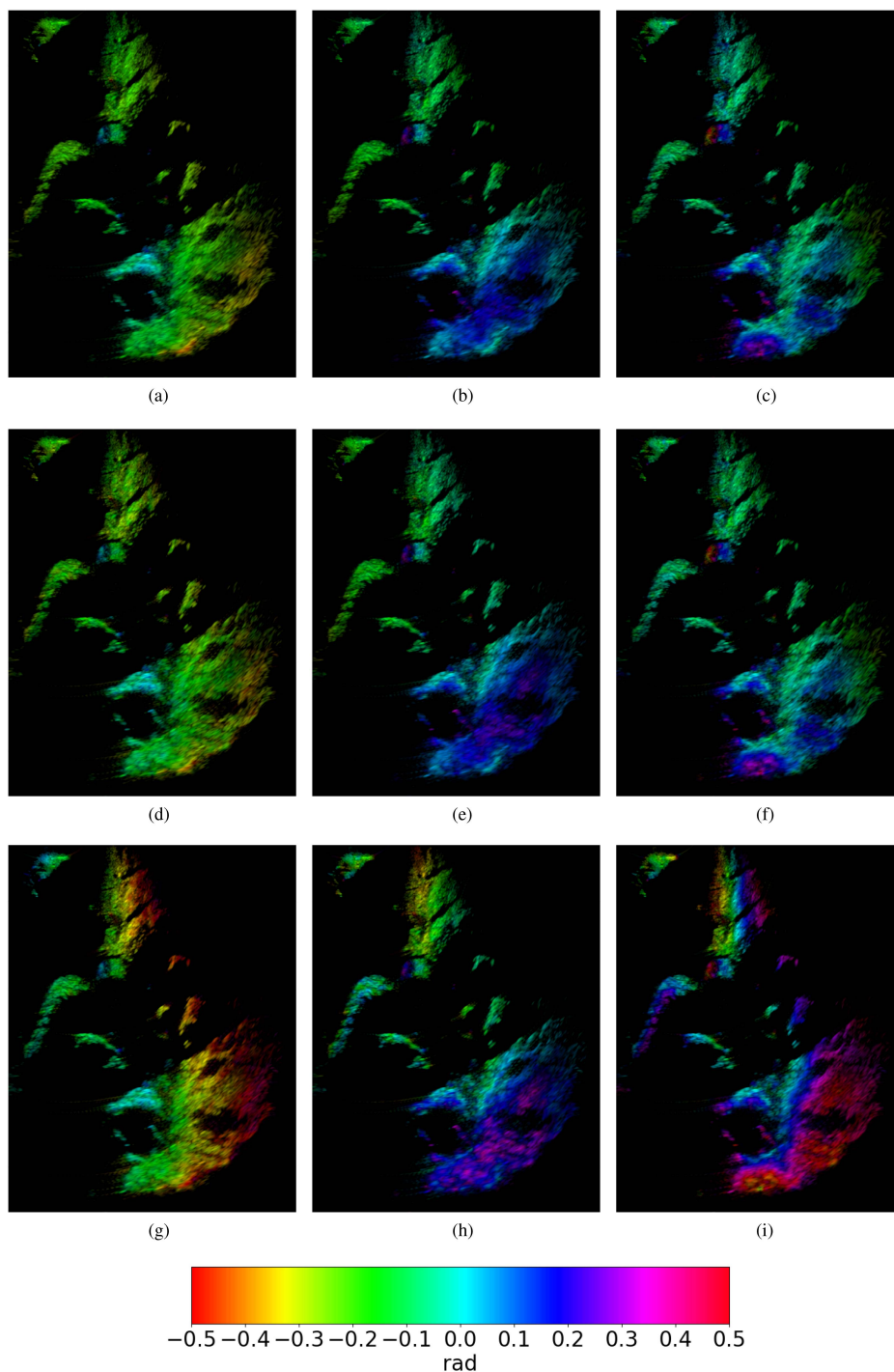
Fig. 13. Repeat-pass DInSAR phase from image pairs focused with the nominal, the RTS local_L1, and the RTS OALP trajectories. Acquisition time indicated in the format HH:MM:SS. The color map is limited to ±0.5 radians to enhance the visibility of the phase errors (out-of-range values are wrapped). The images focused with the nominal and the local_L1 trajectories lead to comparable DInSAR phase while the images focused with the RTS OALP trajectories show additional phase undulations. (a) Trajectories: nominal. Acquisitions: 12:40:39–12:58:42. (b) Trajectories: nominal. Acquisitions: 12:40:39–13:08:00. (c) Trajectories: nominal. Acquisitions: 12:40:39–13:37:46. (d) Trajectories: RTS local_L1. Acquisitions: 12:40:39–12:58:42. (e) Trajectories: RTS local_L1. Acquisitions: 12:40:39–13:08:00. (f) Trajectories: RTS local_L1. Acquisitions: 12:40:39–13:37:46. (g) Trajectories: RTS OALP. Acquisitions: 12:40:39–12:58:42. (h) Trajectories: RTS OALP. Acquisitions: 12:40:39–13:08:00. (i) Trajectories: RTS OALP. Acquisitions: 12:40:39–13:37:46.

errors should be taken into account. DEM offsets have a similar effect as constant positioning offsets and do not pose major problems in the interpretation of the interferograms due to the relative nature of the interferometric measurements [22], [72]. On the other hand, relative height errors between the resolution cells or lateral translations of the DEM occur in addition to positioning errors and can lead to varying phase errors along azimuth and range.

Finally, especially in the case of long temporal baselines, the tropospheric phase error also affect the differential
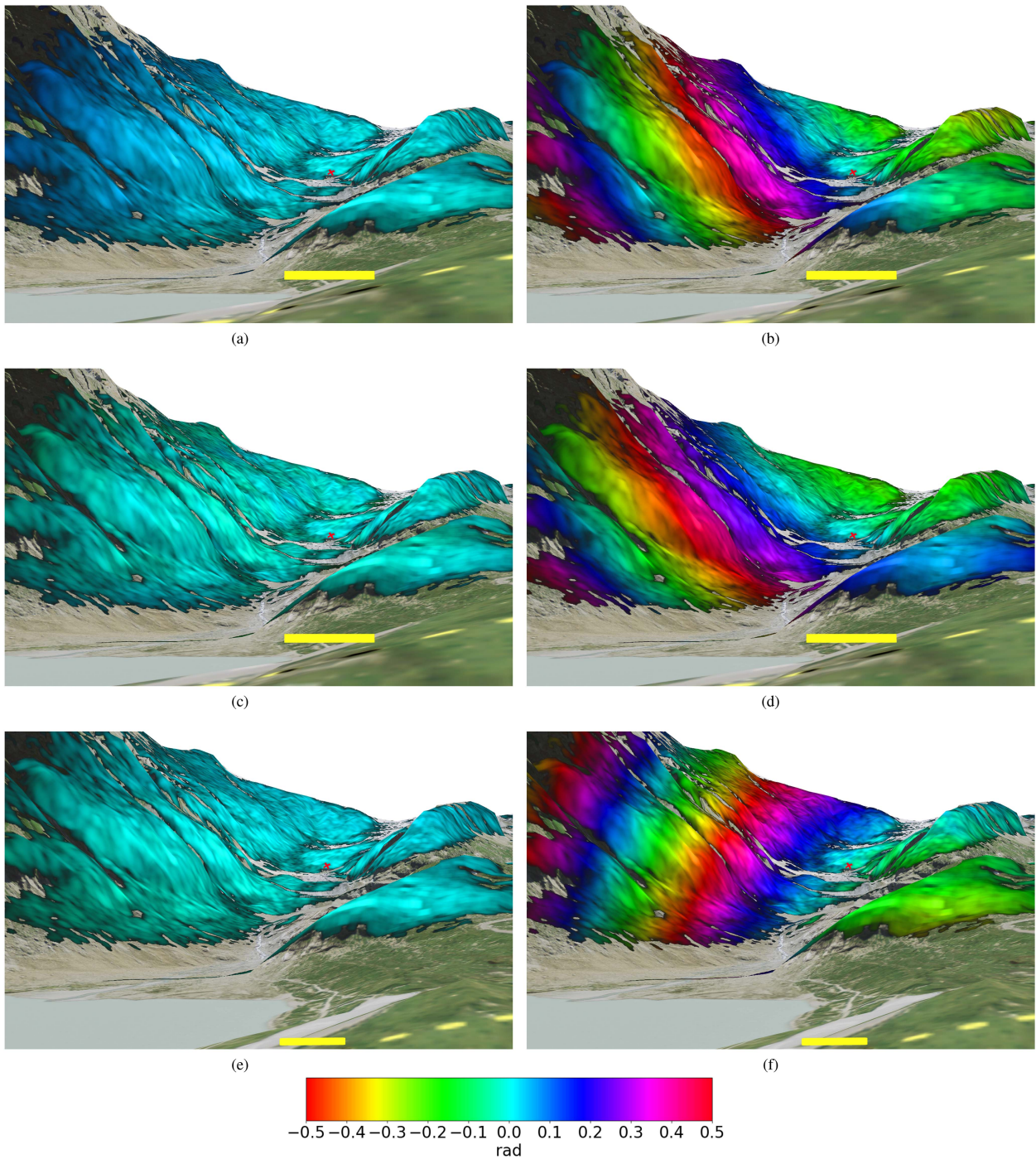
Fig. 14. Phase of the self-interferograms (both SLCs focused from the same raw data) for three different acquisitions. For each self-interferogram, the primary SLC is focused using the nominal trajectory and the secondary SLC is focused using the estimated radar trajectory obtained with the local reference station (RTS local_L1 trajectories) or with the OALP AGNES reference station (RTS OALP trajectories). The color map is limited to ±0.5 radians to enhance the visibility of the phase errors (out-of-range values are wrapped). The dotted yellow line indicates the direction of the rail. The filled yellow line is the average SAR trajectory along the rail (length of 10 m). The red cross is the position of the interferometric reference point. swisstopo geodata. (a) Trajectory: RTS local_L1. Acquisition time: 12:40:39. (b) Trajectory: RTS OALP. Acquisition time: 12:40:39. (c) Trajectory: RTS local_L1. Acquisition time: 12:58:42. (d) Trajectory: RTS OALP. Acquisition time: 12:58:42. (e) Trajectory: RTS local_L1. Acquisition time: 13:37:42. (f) Trajectory: RTS OALP. Acquisition time: 13:37:42.

interferograms and cannot be easily distinguished from uncompensated positioning-related phase errors. Tropospheric phase error are caused by local gradients of the refractive index, which is height dependent and is a function of temperature, pressure, and humidity content of the air and therefore

particularly relevant in the case of steep slopes [69]. As a rough estimate, the differential tropospheric path delays affecting ground-based radar measurements can be in the order of mm/km or cm/km in range [77], [78] which, at L-band, correspond to phase variations between 3°/km and 30°/km or

more, and therefore of comparable order of magnitude with respect to phase trends caused by positioning errors.

## V. CONCLUSION

In this work, trajectory errors experienced between repeated SAR acquisitions and within the time-span of a synthetic aperture with long integration time measured with a navigation-grade INS/GNSS system were analyzed. The analyses, carried out in a controlled rail-based setup with different INS/GNSS configurations, highlighted the positioning performance and the related differential interferometric performance arising from the use of GNSS reference stations at different distances from the radar platform. The controlled rail-based experiment mimics the acquisition scenario of a car-borne DInSAR-based mobile mapping system.

The results showed that the residual positioning errors obtained by relying on the (remote) reference stations of a permanent GNSS network, which are situated at 20 km distance and at a different altitude by several hundred meters compared the measurement site, can be substantial, thus causing nonnegligible residual phase error trends. A significant reduction of the phase errors can be achieved by using a reference station located close to the radar platform, which allows to effectively remove most of the tropospheric disturbance affecting the GNSS signals and to achieve an excellent postprocessed positioning accuracy for repeated passes. This last aspect is particularly relevant in the context of repeat-pass DInSAR acquisitions from agile platforms to avoid as much as possible any disturbing phase trends caused by inaccurate knowledge of the interferometric baseline due to positioning errors, which would otherwise need to be corrected in postprocessing to retrieve the deformation signal with high accuracy.

## REFERENCES

[1] H. A. Zebker and R. M. Goldstein, "Topographic mapping from interferometric synthetic aperture radar observations," *J. Geophys. Res. Solid Earth*, vol. 91, no. B5, pp. 4993–4999, 1986.

[2] A. K. Gabriel, R. M. Goldstein, and H. A. Zebker, "Mapping small elevation changes over large areas: Differential radar interferometry," *J. Geophys. Res.*, vol. 94, no. B7, pp. 9183–9191, 1989.

[3] R. Bamler and P. Hartl, "Synthetic aperture radar interferometry," *Inverse Problems*, vol. 14, pp. 1–54, Aug. 1998.

[4] G. Fornaro, E. Sansosti, R. Lanari, and M. Tesauro, "Role of processing geometry in SAR raw data focusing," *IEEE Trans. Aerosp. Electron. Syst.*, vol. 38, no. 2, pp. 441–454, Apr. 2002.

[5] D. R. Stevens, I. G. Cumming, and A. L. Gray, "Options for airborne interferometric SAR motion compensation," *IEEE Trans. Geosci. Remote Sens.*, vol. 33, no. 2, pp. 409–420, Mar. 1995.

[6] O. Frey, C. Magnard, M. Rüegg, and E. Meier, "Focusing of airborne synthetic aperture radar data from highly nonlinear flight tracks," *IEEE Trans. Geosci. Remote Sens.*, vol. 47, no. 6, pp. 1844–1858, Jun. 2009.

[7] S. Perna, V. Zamparelli, A. Pauciullo, and G. Fornaro, "Azimuth-to-frequency mapping in airborne SAR data corrupted by uncompensated motion errors," *IEEE Geosci. Remote Sens. Lett.*, vol. 10, no. 6, pp. 1493–1497, Nov. 2013.

[8] D. Blacknell et al., "Geometric accuracy in airborne SAR images," *IEEE Trans. Aerosp. Electron. Syst.*, vol. 25, no. 2, pp. 241–258, Mar. 1989.

[9] S. Buckreuss, "Motion errors in an airborne synthetic aperture radar system," *Eur. Trans. Telecommun.*, vol. 2, no. 6, pp. 655–664, 1991.

[10] G. Fornaro, "Trajectory deviations in airborne SAR: Analysis and compensation," *IEEE Trans. Aerosp. Electron. Syst.*, vol. 35, no. 3, pp. 997–1009, Jul. 1999.

[11] G. Fornaro, G. Franceschetti, and S. Perna, "Motion compensation errors: Effects on the accuracy of airborne SAR images," *IEEE Trans. Aerosp. Electron. Syst.*, vol. 41, no. 4, pp. 1338–1352, Oct. 2005.

[12] S. Buckreuss, "Motion compensation for airborne SAR based on inertial data, RDM and GPS," in *Proc. IEEE Int. Geosci. Remote Sens. Symp.*, vol. 4, 1994, pp. 1971–1973.

[13] J. L. Weston and D. H. Titterton, "Modern inertial navigation technology and its application," *Electron. Commun. Eng. J.*, vol. 12, pp. 49–64, Apr. 2000.

[14] D. Titterton and J. L. Weston, *Strapdown Inertial Navigation Technology. Radar, Sonar and Navigation*, London, U.K.: IET, 2004.

[15] A. Reigber and K. Papathanassiou, "Correction of residual motion errors in airborne repeat-pass interferometry," in *Proc. IEEE Int. Geosci. Remote Sens. Symp.*, 2001, vol. 7, pp. 3077–3079.

[16] A. Reigber, P. Prats, and J. Mallorqui, "Refined estimation of time-varying baseline errors in airborne SAR interferometry," *IEEE Geosci. Remote Sens. Lett.*, vol. 3, no. 1, pp. 145–149, Jan. 2006.

[17] P. Prats, A. Reigber, J. J. Mallorqui, and A. Broquetas, "Efficient detection and correction of residual motion errors in airborne SAR interferometry," in *Proc. IEEE Int. Geosci. Remote Sens. Symp.*, 2004, vol. 2, pp. 992–995.

[18] N. Cao et al., "Estimation of residual motion errors in airborne SAR interferometry based on time-domain backprojection and multisquint techniques," *IEEE Trans. Geosci. Remote Sens.*, vol. 56, no. 4, pp. 2397–2407, Apr. 2018.

[19] R. S. Goodman, S. Tummala, and W. G. Carrara, "Issues in ultra-wideband, widebeam SAR image formation," in *Proc. Rec. IEEE Radar Conf.*, 1995, pp. 479–485.

[20] S. N. Madsen, "Motion compensation for ultra wide band SAR," in *Proc. IEEE Int. Geosci. Remote Sens. Symp.*, vol. 3, 2001, pp. 1–3.

[21] A. Reigber, E. Alivizatos, A. Potsis, and A. Moreira, "Extended wavenumber-domain synthetic aperture radar focusing with integrated motion compensation," *IEE Proc.—Radar, Sonar, Navig.*, vol. 153, no. 3, pp. 301–310, 2006.

[22] M. I. Duersch and D. G. Long, "Analysis of time-domain back-projection for stripmap SAR," *Int. J. Remote Sens.*, vol. 36, no. 8, pp. 2010–2036, 2015.

[23] Accuracy (Trueness and Precision) of Measurement Methods and Results-Part 1: General Principles and Definitions, ISO (Int. Organisation for Standardisation), 1994.

[24] D. Lu et al., "Repeatability test method of GNSS for safe train localisation in real and simulated environments," in *Proc. IEEE/ION Position, Location, Navig. Symp.*, 2016, pp. 687–692.

[25] R. Coscione, I. Hajnsek, and O. Frey, "Trajectory uncertainty in repeat-pass SAR interferometry: A case study," in *Proc. IEEE Int. Geosci. Remote Sens. Symp.*, 2019, pp. 338–341.

[26] R. E. Kalman, "A new approach to linear filtering and prediction problems," *J. Basic Eng.*, vol. 82, no. 1, 1960, Art. no. 35.

[27] P. Georgiadou and A. Kleusberg, "On the effect of ionospheric delay on geodetic relative GPS positioning," *J. Geodesy*, vol. 13, no. 1, pp. 1–8, 1988.

[28] H. Nahavandchi and A. Soltanpour, "Local ionospheric modelling of GPS code and carrier phase observations," *Surv. Rev.*, vol. 40, no. 309, pp. 271–284, 2008.

[29] T. Hobiger and N. Jakowski, *Atmospheric Signal Propagation*. Berlin, Germany: Springer, 2017, pp. 165–193.

[30] B. Hofmann-Wellenhof, H. Lichtenegger, and E. Wasle, *GNSS Global Navigation Satellite Syst., GPS, GLONASS, Galileo, and More*. Vienna, Austria: Springer, 2008.

[31] Y. Feng and J. Wang, "GPS RTK performance characteristics and analysis," *J. Glob. Positioning Syst.*, vol. 7, no. 1, pp. 1–8, 2008.

[32] C. Rajasekhar, V. B. S. S. I. Dutt, and G. S. Rao, "Role of optimum satellite-receiver geometry in the accuracy of GPS navigation solution—An investigation," in *Proc. Int. Conf. Commun. Signal Process.*, 2015, pp. 1185–1189.

[33] R. A. Snay and T. Soler, "Continuously operating reference station (cors): History, applications, and future enhancements," *J. Surv. Eng.*, vol. 134, no. 4, pp. 95–104, 2008.

[34] C. Bruyninx et al., *The European Reference Frame: Maintenance and Products*. Berlin, Germany: Springer, 2009, pp. 131–136.

[35] E. Brockmann, S. Grünig, D. Ineichen, and S. Schaer, "Monitoring the automated GPS network of Switzerland AGNES," in *Proc. Rep. Symp. IAG Subcommission Eur.*, vol. 28, 2006, Art. no. 100.

[36] A. Potsis, A. Reigber, J. Mittermayer, A. Moreira, and N. Uzunoglou, "Sub-aperture algorithm for motion compensation improvement in wide-beam SAR data processing," *Electron. Lett.*, vol. 37, no. 23, pp. 1405–1407, 2001.

[37] A. Reigber and R. Scheiber, "Airborne differential SAR interferometry: First results at l-band," *IEEE Trans. Geosci. Remote Sens.*, vol. 41, no. 6 PART II, pp. 1516–1520, Jun. 2003.

[38] K. A. C. de Macedo and R. Scheiber, "Precise topography- and aperture-dependent motion compensation for airborne SAR," *IEEE Geosci. Remote Sens. Lett.*, vol. 2, no. 2, pp. 172–176, Apr. 2005.

[39] P. Prats, A. Reigber, and J. J. Mallorqui, "Topography-dependent motion compensation for repeat-pass interferometric SAR systems," *IEEE Geosci. Remote Sens. Lett.*, vol. 2, no. 2, pp. 206–210, Apr. 2005.

[40] P. Prats, K. A. C. de Macedo, A. Reigber, R. Scheiber, and J. J. Mallorqui, "Comparison of topography- and aperture-dependent motion compensation algorithms for airborne SAR," *IEEE Geosci. Remote Sens. Lett.*, vol. 4, no. 3, pp. 349–353, Jul. 2007.

[41] J. C. Kirk, "Motion compensation for synthetic aperture radar," *IEEE Trans. Aerosp. Electron. Syst.*, vol. AES-11, no. 3, pp. 338–348, May 1975.

[42] J. Moreira, "A new method of aircraft motion error extraction from radar raw data for real time motion compensation," *IEEE Trans. Geosci. Remote Sens.*, vol. 28, no. 4, pp. 620–626, Jul. 1990.

[43] D. Wahl, P. Eichel, D. Ghiglia, and C. Jakowatz, "Phase gradient autofocus—A robust tool for high resolution SAR phase correction," *IEEE Trans. Aerosp. Electron. Syst.*, vol. 30, no. 3, pp. 827–835, Jul. 1994.

[44] W. G. Carrara, R. S. Goodman, and R. M. Majewski, *Spotlight Synthetic Aperture Radar: Signal Processing Algorithms*. Norwood, MA, USA: Artech House, 1995.

[45] H. M. J. Cantalloube and C. E. Nahum, "Autofocusing of (inverse) synthetic aperture radar for motion compensation," in *Proc. IEEE Nat. Aerosp. Electron. Conf.*, 1996, pp. 309–316.

[46] H. M. Cantalloube and C. E. Nahum, "Multiscale local map-drift-driven multilateration SAR autofocus using fast polar format image synthesis," *IEEE Trans. Geosci. Remote Sens.*, vol. 49, no. 10, pp. 3730–3736, Oct. 2011.

[47] P. Decroix, X. Neyt, and M. Acheroy, "Trade-off between motion measurement accuracy and autofocus capabilities in airborne SAR motion compensation," in *Proc. 2nd Microw. Radar Week Poland - Int. Radar Symp.*, 2006, pp. 1–4.

[48] K. A. C. de Macedo, R. Scheiber, and A. Moreira, "An autofocus approach for residual motion errors with application to airborne repeat-pass SAR interferometry," *IEEE Trans. Geosci. Remote Sens.*, vol. 46, no. 10, pp. 3151–3162, Oct. 2008.

[49] O. Frey, C. L. Werner, U. Wegmüller, A. Wiesmann, D. Henke, and C. Magnard, "A car-borne SAR and InSAR experiment," in *Proc. IEEE Int. Geosci. Remote Sens. Symp.*, 2013, pp. 93–96.

[50] R. Coscione, I. Hajnsek, and O. Frey, "An experimental car-borne SAR system: Measurement setup and positioning error analysis," in *Proc. IEEE Int. Geosci. Remote Sens. Symp.*, 2018, pp. 6364–6367.

[51] O. Frey, C. L. Werner, I. Hajnsek, and R. Coscione, "A car-borne SAR system for interferometric measurements: Development status and system enhancements," in *Proc. IEEE Int. Geosci. Remote Sens. Symp.*, 2018, pp. 6508–6511.

[52] O. Frey, C. Werner, and R. Coscione, "Car-borne and UAV-borne mobile mapping of surface displacements with a compact repeat-pass interferometric SAR system at l-band," in *Proc. IEEE Int. Geosci. Remote Sens. Symp.*, 2019, pp. 274–277.

[53] O. Frey, C. L. Werner, A. Manconi, and R. Coscione, "Measurement of surface displacements with a UAV-borne/car-borne l-band DInSAR system: System performance and use cases," in *Proc. IEEE Int. Geosci. Remote Sens. Symp.*, 2021, pp. 628–631.

[54] P. D. Groves, "Principles of GNSS, inertial, and multisensor integrated navigation systems," in *GNSS Technology and Applications Series*, 2nd ed., Boston, MA, USA: Artech House, 2013.

[55] H. E. Rauch, C. T. Striebel, and F. Tung, "Maximum likelihood estimates of linear dynamic systems," *AIAA J.*, vol. 3, pp. 1445–1450, Aug. 1965.

[56] E. L. v. Hinüber, C. Reimer, T. Schneider, and M. Stock, "INS/GNSS integration for aerobatic flight applications and aircraft motion surveying," *Sensors (Switzerland)*, vol. 17, Apr. 2017, Art. no. 941.

[57] C. M. Silva, D. B. Alves, E. M. Souza, and P. T. Setti Junior, "Ionospheric scintillation impact on ambiguity resolution using ADOP in closed form," *Adv. Space Res.*, vol. 64, pp. 921–932, Aug. 2019.

[58] A. E.-S. El-Rabbany, "The effect of physical correlations on the ambiguity resolution and accuracy estimation in GPS differential positioning," Ph.D. dissertation, Dept. Geodesy Geomatics Eng., Univ. New Brunswick, Fredericton, Canada, Tech. Rep. 170, 1994.

[59] C. Miller, K. O. Keefe, and Y. Gao, "Time correlation in GNSS positioning over short baselines," *J. Surv. Eng.*, vol. 138, no. 1, pp. 17–24, 2012.

[60] M. Soumekh, *Synthetic Aperture Radar Signal Processing: With MATLAB Algorithms*. Hoboken, NJ, USA: Wiley, 1999.

[61] L. Ulander, H. Hellsten, and G. Stenstrom, "Synthetic-aperture radar processing using fast factorized back-projection," *IEEE Trans. Aerosp. Electron. Syst.*, vol. 39, no. 3, pp. 760–776, Jul. 2003.

[62] O. Frey, E. Meier, and D. Nüesch, "Processing SAR data of rugged terrain by time-domain back-projection," *Proc. SPIE*, 2005, vol. 5980, pp. 71–79.

[63] O. Frey, C. L. Werner, and U. Wegmüller, "GPU-based parallelized time-domain back-projection processing for agile SAR platforms," in *Proc. IEEE Int. Geosci. Remote Sens. Symp.*, 2014, pp. 1132–1135.

[64] J. Torgrimsson, P. Dammert, H. Hellsten, and L. M. H. Ulander, "SAR processing without a motion measurement system," *IEEE Trans. Geosci. Remote Sens.*, vol. 57, no. 2, pp. 1025–1039, Feb. 2019.

[65] A. Ribalta, "Time-domain reconstruction algorithms for FMCW-SAR," *IEEE Geosci. Remote Sens. Lett.*, vol. 8, no. 3, pp. 396–400, May 2011.

[66] G. Nico, D. Leva, G. Antonello, and D. Tarchi, "Ground-based SAR interferometry for terrain mapping: Theory and sensitivity analysis," *IEEE Trans. Geosci. Remote Sens.*, vol. 42, no. 6, pp. 1344–1350, Jun. 2004.

[67] R. Caduff, F. Schlunegger, A. Kos, and A. Wiesmann, "A review of terrestrial radar interferometry for measuring surface change in the geosciences," *Earth Surf. Process. Landforms*, vol. 40, no. 2, pp. 208–228, 2015.

[68] S. Placidi, A. Meta, L. Testa, and S. Rödelsperger, "Monitoring structures with FastGBSAR," in *Proc. IEEE Radar Conf.*, 2015, pp. 435–439.

[69] R. F. Hanssen, *Radar Interferometry: Data Interpretation and Error Analysis. Remote Sensing and Digital Image Processing*. Berlin, Germany: Springer, 2001.

[70] P. A. Rosen et al., "Synthetic aperture radar interferometry," *Proc. IEEE*, vol. 88, no. 3, pp. 333–382, Mar. 2000.

[71] H. Ku, "Notes on the use of propagation of error formulas," *J. Res. Nat. Bur. Standards, Sect. C, Eng. Instrum.*, vol. 70C, Oct. 2012, Art. no. 263.

[72] H. Bähr and R. F. Hanssen, "Reliable estimation of orbit errors in spaceborne SAR interferometry," *J. Geodesy*, vol. 86, pp. 1147–1164, May 2012.

[73] A. Pepe and F. Caló, "A review of interferometric synthetic aperture radar (inSAR) multi-track approaches for the retrieval of Earth's surface displacements," *Appl. Sci.*, vol. 7, no. 12, 2017, Art. no. 1264.

[74] Z. Wang, Z. Li, and J. Mills, "Modelling of instrument repositioning errors in discontinuous multi-campaign ground-based SAR (MC-GBSAR) deformation monitoring," *ISPRS J. Photogrammetry Remote Sens.*, vol. 157, pp. 26–40, Nov. 2019.

[75] C. Hu, J. Zhu, Y. Deng, W. Tian, and P. Yin, "Repositioning error compensation in discontinuous ground-based SAR monitoring," *Remote Sens.*, vol. 13, Jun. 2021, Art. no. 2461.

[76] O. Monserrat, M. Crosetto, and G. Luzi, "A review of ground-based SAR interferometry for deformation measurement," *ISPRS J. Photogrammetry Remote Sens.*, vol. 93, pp. 40–48, 2014.

[77] L. Iannini and A. Monti Guarnieri, "Atmospheric phase screen in ground-based radar: Statistics and compensation," *IEEE Geosci. Remote Sens. Lett.*, vol. 8, no. 3, pp. 537–541, May 2011.

[78] R. Iglesias et al., "Atmospheric phase screen compensation in ground-based SAR with a multiple-regression model over mountainous regions," *IEEE Trans. Geosci. Remote Sens.*, vol. 52, no. 5, pp. 2436–2449, May 2014.